



Fracture propagation in 3D by the symmetric Galerkin boundary element method

A. FRANGI

Department of Structural Engineering, Politecnico of Milano, P.za L. da Vinci 92, 20133 Milan, Italy (E-mail: attilio.frangi@polimi.it)

Received 14 August 2001; accepted in revised form 27 May 2002

Abstract. The numerical simulation of fatigue crack propagation in 3D linear elastic bodies is addressed. The symmetric Galerkin BEM is employed, thus drastically reducing the remeshing work compared to what is needed by domain formulations. The propagation algorithm adopted has been implemented into a fully automated numerical code and utilized to analyze two examples concerning surface breaking cracks.

Key words: variational BEM, linear elastic fracture mechanics, fracture propagation

1. Introduction

The numerical simulation of fracture propagation in three dimensions is still a challenging problem mainly due to the need for efficient remeshing strategies to be employed as the crack evolves; this issue limits the applicability of domain methods like the FEM and it has so far prevented the development of completely automated and robust routines.

The boundary element method greatly reduces this difficulty since remeshing is required only along the crack front and where the crack front intersects the outer surface. A few contributions have appeared recently concerning crack-growth simulations using boundary elements (see e.g. Li and Keer, 1992, Mi and Aliabadi, 1994, Mi, 1996, Carter *et al.*, 2000, Xu and Ortiz, 1993). In some cases pure Mode I behaviour is assumed or the subregion approach is employed in order to circumvent difficulties arising in fracture mechanics. In other more advanced applications (Mi and Aliabadi, 1994, Mi, 1996, Cisilino and Aliabadi, 1997) the dual approach is adopted: essentially this formulation enforces the traction equation (in addition to the traditional Somigliana displacement identity) at points of the fracture surface. However, strong continuity requirements are set on the displacement fields (C^1 continuity, essentially) at the collocation points. This has led either to the introduction of non-conforming elements (which however entail a certain loss of accuracy especially near the crack front) or to the adoption of special interpolation techniques (see e.g. Wilde and Aliabadi, 1999).

All these difficulties are elegantly circumvented by the symmetric Galerkin approach (SGBEM) which has been recently implemented for the simulation of 3D fractures in elasticity by Li *et al.* (1998) and Frangi *et al.* (2002). This variational method yields symmetric coefficient matrices and generally provides high accuracy and better convergence properties especially when iterative solvers are employed (see e.g. Yoshida *et al.*, 2001). Starting from these experiences the SGBEM is here applied to simulate fracture propagation, envisaging the simple case of fatigue at high number of cycles governed by a naïf propagation criterion.

A detailed explanation of the theoretical background for the SGBEM can be found e.g. in Bonnet *et al.* (1998), Frangi (1998), Li *et al.* (1998) and is only briefly recalled in the sequel.

Let Ω denote a generic body of boundary S in the orthonormal cartesian reference system (x_1, x_2, x_3) , subject to tractions $p_i(\mathbf{x}) = \bar{p}_i(\mathbf{x})$ on S_p , with displacements $u_i(\mathbf{x}) = \bar{u}_i(\mathbf{x})$ enforced on $S_u = S/S_p$. Let surface S_c denote a crack inside Ω , conceived as a locus of displacement discontinuity $w(\mathbf{x}) = u(\mathbf{x}^+) - u(\mathbf{x}^-)$, with $\mathbf{x}^+ \in S_c^+$ and $\mathbf{x}^- \in S_c^-$, S_c^+ and S_c^- being the upper and lower faces of the crack. The positive orientation of S_c is associated with the normal unit vector to S_c pointing from S_c^- to S_c^+ . Equal and opposite tractions can be applied to the crack surfaces: $p_i(\mathbf{x}) \equiv p_i(\mathbf{x}^-) = -p_i(\mathbf{x}^+)$ on S_c .

Two different integral equations serve as starting point for the formulation of the SGBEM: the classical Somigliana equation

$$u_i(\tilde{\mathbf{x}}) = \int_S [G_{ik}^{uu}(\mathbf{x} - \tilde{\mathbf{x}}) p_k(\mathbf{x}) - G_{ikj}^{u\sigma}(\mathbf{x} - \tilde{\mathbf{x}}) n_j u_k(\mathbf{x})] dS_x + \int_{S_c} G_{ikj}^{u\sigma}(\mathbf{x} - \tilde{\mathbf{x}}) n_j w_k(\mathbf{x}) dS_x \quad (1)$$

and the ‘traction’ equation

$$p_i(\tilde{\mathbf{x}}) = \int_S [G_{ijk}^{\sigma u}(\mathbf{x} - \tilde{\mathbf{x}}) \tilde{n}_j(\tilde{\mathbf{x}}) p_k(\mathbf{x}) - G_{ijkp}^{\sigma\sigma}(\mathbf{x} - \tilde{\mathbf{x}}) \tilde{n}_j(\tilde{\mathbf{x}}) n_p(\mathbf{x}) u_k(\mathbf{x})] dS_x + \int_{S_c} G_{ijkp}^{\sigma\sigma}(\mathbf{x} - \tilde{\mathbf{x}}) \tilde{n}_j(\tilde{\mathbf{x}}) n_p(\mathbf{x}) w_k(\mathbf{x}) dS_x \quad (2)$$

Indeed, Equations (1) and (2) hold for a generic point $\tilde{\mathbf{x}} \in \Omega$ the two-point Kelvin kernel $G_{ik}^{uu}(\mathbf{x} - \tilde{\mathbf{x}}) p_k(\mathbf{x})$ expresses the displacement at \mathbf{x} in the k th direction due to a concentrated force acting at $\tilde{\mathbf{x}}$ in the i th direction:

$$G_{ik}^{uu}(\mathbf{x} - \tilde{\mathbf{x}}) p_k(\mathbf{x}) = \frac{1}{16\pi\mu(1-\nu)} \frac{1}{r} [(3-4\nu)\delta_{ik} + r_{,i}r_{,k}] \quad (3)$$

Kernel $G_{ikj}^{u\sigma}(\mathbf{x} - \tilde{\mathbf{x}})$ denotes the kj component of stresses at \mathbf{x} due to the same source, obtained by differentiation of G_{ik}^{uu} and application of Hooke’s law, C_{kijm} being the elastic stiffness tensor:

$$G_{ikj}^{u\sigma}(\mathbf{x} - \tilde{\mathbf{x}}) = C_{kijm} G_{im,n}^{uu}(\mathbf{x} - \tilde{\mathbf{x}}). \quad (4)$$

Moreover

$$G_{ikj}^{\sigma u} = C_{ijab} G_{ak,b}^{uu} \quad G_{ijkp}^{\sigma\sigma} = C_{ijab} C_{kpca} G_{ac,b}^{uu} \quad (5)$$

are the so-called Gebbia kernels (see Bonnet *et al.*, 1998). Unit vector \mathbf{n} defines the outward normal to S at point \mathbf{x} while $\tilde{\mathbf{n}}$ defines a reference normal associated to $\tilde{\mathbf{x}}$; symbol $(\cdot)_{,i}$ denotes differentiation with respect to \tilde{x}_i .

In customary collocation approaches Equations (1) and (2) are enforced pointwise at given points on the boundary with $\tilde{\mathbf{n}}$ in Equation (2) being set equal to the actual outward normal at the collocation boundary point. In view of the singular nature of kernels for $\tilde{\mathbf{x}} \rightarrow \mathbf{x}$, an

infinitesimal domain Ω_ε (of linear dimension ε) is often excluded from Ω and the limit for $\varepsilon \rightarrow 0$ is analysed.

A totally different approach is followed in the symmetric Galerkin method. Let us introduce a surface \tilde{S} representing a fictitious contour *internal* to Ω . We assume the existence of a one-to-one correspondence between points $\mathbf{x} \in S$ and $\tilde{\mathbf{x}} \in \tilde{S} : \tilde{\mathbf{x}} = \chi(\mathbf{x}, h)$, where h is a parameter such that $\mathbf{x} = \chi(\mathbf{x}, 0)$. Hence the two surfaces coincide for $h = 0$. In particular \tilde{S} will consist of portions \tilde{S}_u, \tilde{S}_p and, in the presence of an internal crack, also of $\tilde{S}_c^+, \tilde{S}_c^-$ mapped by one-to-one correspondence onto the respective portions of S and of S_c .

The procedure basically consists of two distinct steps: first Equations (1) and (2) are enforced in a weak sense on the auxiliary contour \tilde{S} *distinct* from S (i.e. with $h \neq 0$) and an analytical regularization procedure is performed via integration by parts removing all higher-order singularities. Secondly, the limit $S \rightarrow \tilde{S}$ ($h \rightarrow 0$) is performed and the discretization procedure is initiated. The definition of an auxiliary surface \tilde{S} separated from S is hence only an artifice which proves useful in the rather involved issue of guaranteeing a firm mathematical and computational basis for the evaluation of the singular double integrals involved; however \tilde{S} does not play any role in the final implementation of the method, since for $h \rightarrow 0$, $\tilde{S} \equiv S$.

More specifically Equation (1) is enforced on \tilde{S}_u using as test function the static field $\tilde{p}_i(\tilde{\mathbf{x}})$ while Equation (2) is enforced both on \tilde{S}_p and on \tilde{S}_c using as test function the kinematic field \tilde{u}_i . By applying the regularization procedure detailed by Bonnet (1993), Frangi (1991) and Bonnet *et al.* (1998), and taking the limit $\tilde{S} \rightarrow S$ (hence $h \rightarrow 0$), the variational equations listed in the following paragraphs are obtained.

1.1. REGULARIZED WEAK FORM OF THE DISPLACEMENT INTEGRAL EQUATION ON S_u

$$\begin{aligned} \frac{1}{2} \int_{S_u} u_i(\mathbf{x}) \tilde{p}_i(\mathbf{x}) dS_x = & \int_{S_u} \int_S \tilde{p}_i(\tilde{\mathbf{x}}) G_{ik}^{uu}(\mathbf{x} - \tilde{\mathbf{x}}) p_k(\mathbf{x}) dS_x dS_{\tilde{x}} \\ & + \int_{S_u} \int_S \tilde{p}_i(\tilde{\mathbf{x}}) \left[\frac{1}{4\pi} \frac{1}{r^2} r_{,i} n_i(\mathbf{x}) u_i(\mathbf{x}) + G_{ikj}^{u\varphi}(\mathbf{x} - \tilde{\mathbf{x}}) R_j[u_k](\mathbf{x}) \right] dS_x dS_{\tilde{x}} \\ & - \int_{S_u} \int_{S_c} \tilde{p}_i(\tilde{\mathbf{x}}) \left[\frac{1}{4\pi} \frac{1}{r^2} r_{,i} n_i(\mathbf{x}) w_i(\mathbf{x}) + G_{ikj}^{u\varphi}(\mathbf{x} - \tilde{\mathbf{x}}) R_j[w_k](\mathbf{x}) \right] dS_x dS_{\tilde{x}} \end{aligned} \quad (6)$$

where

$$G_{ikj}^{u\varphi}(\mathbf{x} - \tilde{\mathbf{x}}) = \frac{1}{8\pi(1-\nu)r} [(1-2\nu)e_{ikj} - e_{ipj}r_{,p}r_{,k}], \quad (7)$$

and R_j denotes the surface curl operator (see Bonnet *et al.*, 1998):

$$R_j[u_k](\mathbf{x}) = e_{bcj} n_b(\mathbf{x}) \frac{\partial u_k}{\partial x_c}(\mathbf{x}) \quad (8)$$

It should be stressed that both G^{uu} and the auxiliary kernel $G^{u\varphi}$ are weakly singular; the additional terms in Equation (6) (which coincide with the double layer kernel for potential problems) are, in actual fact, weakly singular as well since

$$\frac{1}{r^2} r_{,i} n_i dS_x = d\Theta$$

represents the differential solid angle under which dS_x is seen from $\tilde{\mathbf{x}}$.

1.2. REGULARIZED WEAK FORM OF THE TRACTION INTEGRAL EQUATION ON S_p

$$\begin{aligned} \frac{1}{2} \int_{S_p} p_i(\mathbf{x}) \tilde{u}_i(\mathbf{x}) dS_x &= \int_{S_p} \int_S \left[-\frac{1}{4\pi} \tilde{u}_i(\tilde{\mathbf{x}}) \frac{1}{r^2} r_{,\tilde{p}} \tilde{n}_p(\tilde{\mathbf{x}}) p_i(\mathbf{x}) \right. \\ &\quad - \tilde{R}_j[\tilde{u}_i](\tilde{\mathbf{x}}) G_{ijk}^{\varphi u}(\mathbf{x} - \tilde{\mathbf{x}}) p_k(\mathbf{x}) \\ &\quad \left. - \tilde{R}_j[\tilde{u}_i](\tilde{\mathbf{x}}) G_{ijkq}^{\varphi\varphi}(\mathbf{x} - \tilde{\mathbf{x}}) R_q[u_k](\mathbf{x}) \right] dS_x dS_{\tilde{x}} \\ &\quad + \int_{S_p} \int_S \tilde{R}_j[\tilde{u}_i](\tilde{\mathbf{x}}) G_{ijkq}^{\varphi\varphi}(\mathbf{x} - \tilde{\mathbf{x}}) R_q[w_k](\mathbf{x}) dS_x dS_{\tilde{x}} \end{aligned} \quad (9)$$

where:

$$G_{ikj}^{\varphi u} = \frac{1}{8\pi(1-\nu)r} [(1-2\nu)e_{kij} - e_{kpj}r_{,p}r_{,i}] \quad (10)$$

$$G_{ijkq}^{\varphi\varphi} = -\frac{\mu}{8\pi} \frac{1}{r} (\delta_{eg} - r_{,e}r_{,g}) e_{iep} e_{jgr} \left[\frac{2\nu}{1-\nu} \delta_{pk} \delta_{rq} + \delta_{pr} \delta_{kq} + \delta_{pq} \delta_{kr} \right]$$

and:

$$\tilde{R}_j[\tilde{u}_i](\tilde{\mathbf{x}}) = e_{bcj} \tilde{n}_b(\tilde{\mathbf{x}}) \frac{\partial u_k}{\partial x_c}(\mathbf{x})$$

$$\frac{1}{r^2} r_{,i} \tilde{n}_i dS_{\tilde{x}} = d\tilde{\Theta}$$

$d\tilde{\Theta}$ represents the differential solid angle under which $dS_{\tilde{x}}$ is seen from \mathbf{x} . Hence, also all the kernels in Equation (9) are weakly singular.

1.3. REGULARIZED WEAK FORM FOR THE TRACTION INTEGRAL EQUATION ON S_c

If we define the auxiliary displacement discontinuity field $\tilde{w}_i = \tilde{u}_i^+ - \tilde{u}_i^-$ (naturally flowing from the \tilde{u}_i field after the limit process $h \rightarrow 0$ forces S^+ to coincide with S^-) the variational traction equation on S_c can be written as:

$$\begin{aligned} \int_{S_c} p_i(\mathbf{x}) \tilde{w}_i(\mathbf{x}) dS_x &= \int_{S_c} \int_S \left[-\frac{1}{4\pi} \tilde{w}_i(\mathbf{x}) \frac{1}{r^2} r_{,\tilde{p}} \tilde{n}_p(\tilde{\mathbf{x}}) p_i(\mathbf{x}) \right. \\ &\quad - \tilde{R}_j[\tilde{w}_i](\tilde{\mathbf{x}}) G_{ijk}^{\varphi u}(\mathbf{x} - \tilde{\mathbf{x}}) p_k(\mathbf{x}) \\ &\quad \left. - \tilde{R}_j[\tilde{w}_i](\tilde{\mathbf{x}}) G_{ijkq}^{\varphi\varphi}(\mathbf{x} - \tilde{\mathbf{x}}) R_q[u_k](\mathbf{x}) \right] dS_x dS_{\tilde{x}} \\ &\quad + \int_{S_c} \int_S \tilde{R}_j[\tilde{w}_i](\tilde{\mathbf{x}}) G_{ijkq}^{\varphi\varphi}(\mathbf{x} - \tilde{\mathbf{x}}) R_q[w_k](\mathbf{x}) dS_x dS_{\tilde{x}} \end{aligned} \quad (11)$$

1.4. CONTINUITY REQUIREMENTS

Weak continuity requirements must be enforced on $u_k, w_k, \tilde{u}_k, \tilde{w}_k$ to guarantee the validity of Equations (6)–(11), since they must belong to the class of $C_0^0(S)$ continuous functions. The class $C_0^0(S)$ is defined as follows: $C_0^0(S) \equiv C^0(S)$ if S is closed, and $C_0^0(S) = \{f(\mathbf{x}) \in C^0(S) : f|_{\partial S} = 0\}$ if S is open (e.g. admissible kinematic fields for cracks inside bodies are assumed to be in $C_0^0(S)$). On the contrary no special constraints are set on the static fields p_k and \tilde{p}_k .

The set of the three previous equations generates a self-adjoint bilinear form:

$$\mathcal{A}(\tilde{\mathbf{u}}, \tilde{\mathbf{p}}, \tilde{\mathbf{w}}, \mathbf{u}, \mathbf{p}, \mathbf{w}) = f(\tilde{\mathbf{u}}, \tilde{\mathbf{p}}, \tilde{\mathbf{w}}, \bar{\mathbf{u}}, \bar{\mathbf{p}}) \quad (12)$$

with

$$\mathcal{A}(\tilde{\mathbf{u}}, \tilde{\mathbf{p}}, \tilde{\mathbf{w}}, \mathbf{u}, \mathbf{p}, \mathbf{w}) = \mathcal{A}(\mathbf{u}, \mathbf{p}, \mathbf{w}, \tilde{\mathbf{u}}, \tilde{\mathbf{p}}, \tilde{\mathbf{w}})$$

Through the adoption of a Galerkin discretization scheme, Equation (12) leads to a symmetric linear equation system.

2. Numerical simulations

The evaluation of double surface integrals in Equation (12) represents probably the main obstacle which has hampered the application of the method in the 3D context (see e.g. Sirtori *et al.*, 1992; Balakrishna *et al.*, 1994; Frangi and Novati, 1996 for 2D problems).

However, recent results obtained by applied mathematicians (Andrä and Schnack, 1997; Erichsen and Sauter, 1998; Sauter and Schwab, 1997) have led to innovative algorithms which are now being adopted by the engineering BE community and have served as a basis for the fracture-oriented implementation of the SGBEM in 3D recently presented by Frangi *et al.* (2002) where a few classical benchmark cases have been addressed.

In this paper the extension to the simulation of fracture propagation is considered.

The initial configuration of the crack is assigned and the SGBEM is employed to carry out a stress analysis.

In Section 2.3 (elliptical crack in the unbounded domain) 9-node quarter point elements are employed along the crack front; on the contrary, in Sections 2.4 and 2.5 (surface breaking cracks) only standard 9-node lagrangian elements are utilized, in view of the considerable accuracy shown in Frangi *et al.* (2002) and of the remarks collected in Section 3.

Stress intensity factors are extrapolated using Williams expansion formulae exploiting the displacement discontinuity field evaluated at the nodes of the crack-front elements.

The incremental growth is determined on the basis of a local ‘stress’ criterion; accordingly, a row of boundary elements is then added ahead of the crack front and another analysis cycle is carried out for the new configuration after performing the necessary modifications of the surface mesh as detailed in the sequel. This incremental analysis is repeated until a predefined crack length is reached or the SIFs exceed the fracture toughness of the material, i.e. when unstable propagation of the fracture occurs.

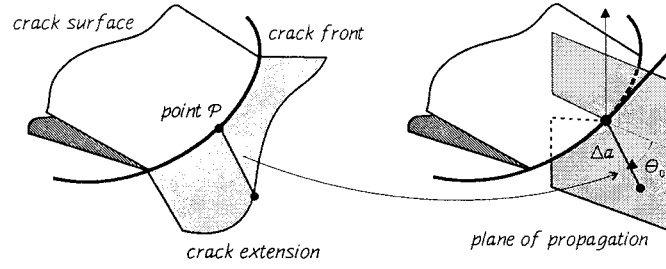


Figure 1. Choice of local crack propagation direction.

2.1. PROPAGATION CRITERION

The formulation of a suitable 3D crack growth criterion, even in the classical context of linear fracture mechanics, still represents an open issue. In this contribution we have chosen to explore potentialities of the SGBEM by simulating a fatigue crack growth governed by a simple Paris law independent of the fatigue ratio R and by a local stress criterion for the selection of the propagation direction. Local and global energy approaches are currently been implemented (see Section 3).

The procedure can be summarized as follows (for further details and alternative choices see, e.g., Mi, 1996): (i) each geometrical point on the crack front moves in the plane perpendicular to the crack front itself (see Figure 1b); (ii) the propagation angle in this plane is determined through an extension of the classical 2D criterion of the maximum hoop stress:

$$\tan \frac{\theta_0}{2} = \frac{1}{4} \left[\frac{K_{I_{eff}}}{K_{II}} \pm \sqrt{\left(\frac{K_{I_{eff}}}{K_{II}} \right)^2 + 8} \right] \quad (13)$$

where $K_{I_{eff}} = K_I + B|K_{III}|$ is an ‘effective’ or ‘equivalent’ mode I SIF also (partially) accounting for the presence of non-zero K_{III} , B being a material parameter; (iii) the advancement length Δa flows from an application of the Paris law:

$$\frac{\Delta a}{\Delta n} = C(\Delta K_{eff})^m \quad (14)$$

where n denotes the number of load-cycles, C and m are material parameters

$$\Delta K_{eff} = K_{eff}^{max} - K_{eff}^{min} \quad K_{eff}^2 = K_{I_{eff}}^2 + 2K_{II}^2 \quad (15)$$

At each step the crack extension is scaled according to the following two criteria: (i) the maximum extension size should not exceed a given fixed value; (ii) the trace of the fracture advancement on the outer surface itself (in the case of a surface breaking crack) should be completely contained in one element, as in Figure 2. The number of load cycles corresponding to the computed amount of incremental extension of the crack can be evaluated using Paris law.

2.2. REMESHING STRATEGY

Let us consider Figure 2 and suppose that: (i) point A is an intersection of the old crack front with the outer surface (‘surface crack tip’); (ii) according to the propagation algorithm the new surface crack tip B lies at some given point of the shaded element (‘propagation element’).

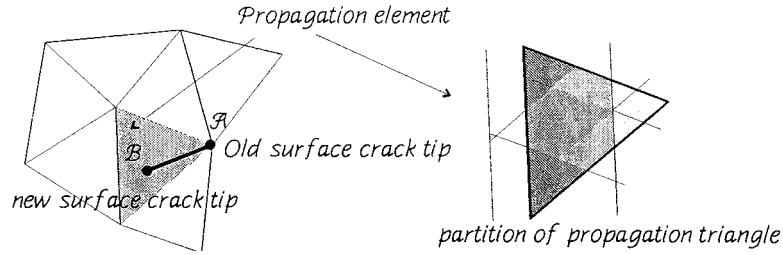


Figure 2. Old and new surface crack tips and partition of propagation element.

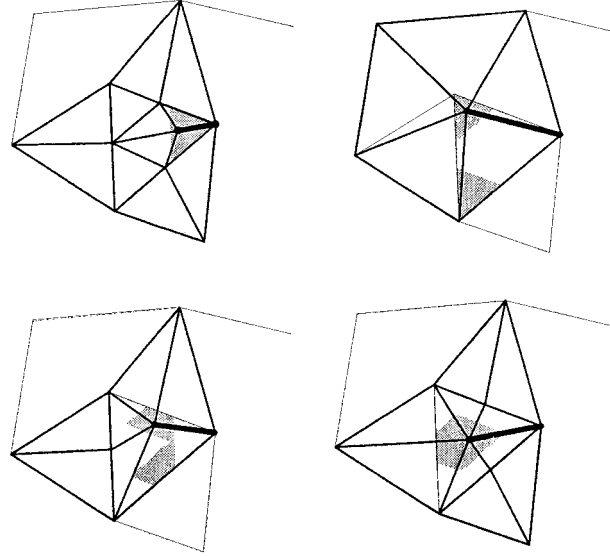


Figure 3. Remeshing techniques adopted: different strategies according to the position of point B in the propagation element. The shaded portions of the propagation triangle correspond to different regions evidenced in Figure 2.

The propagation element is partitioned as in Figure 2b and according to the position of point B different remeshing strategies are adopted, as evidenced in Figure 3.

Since the remeshing algorithm adopted might create poorly shaped triangles, especially at later stages of the propagation process, the next step consists in optimizing the shape of triangles on the outer surface in the vicinity of the crack front. The number of elements which get modified at this stage should be as limited as possible in order to reduce the cost of computing new entries in the coefficient matrix. Hence only the position of the nodes that share a triangle side with the new surface crack tip nodes ('near-tip nodes') is modified.

Moreover elements adjacent to the crack tip get generally more distorted in the remeshing procedure; since these are crucial in obtaining a satisfactory response in terms of displacement discontinuity, the objective function to be minimized also includes a weight factor λ_{el} for each element, with λ_{el} varying according to the mean distance of the element from the surface crack tip node. The choice adopted in the code developed is to set $\lambda_{el} = 3$ if an element contains a surface crack tip node as vertex, $\lambda_{el} = 1$ if it contains at least one near-tip node, and $\lambda_{el} = 0$ otherwise.

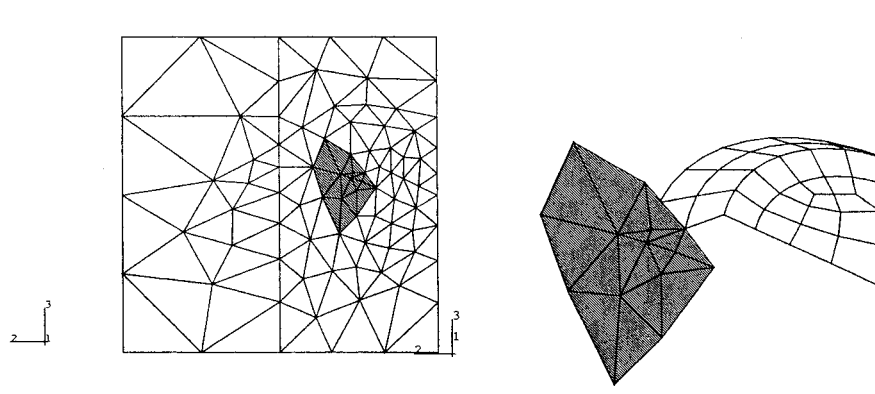


Figure 4. Elements around surface crack tip before smoothing.

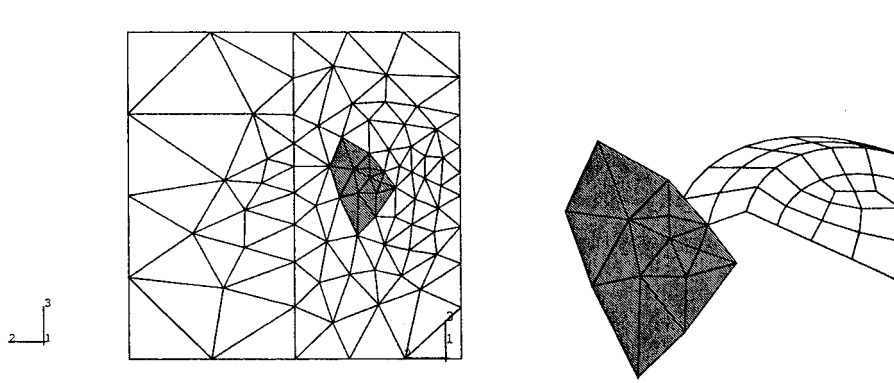


Figure 5. Elements around surface crack tip after smoothing.

The selected objective function eventually is:

$$\mathcal{F} = \sum_{\text{elements}} \lambda_{\text{el}} \sum_{\text{vertices}} \frac{(\pi/3 - \alpha_{\text{ver}})^2}{\sqrt{|\alpha_{\text{ver}}(\pi - \alpha_{\text{ver}})|}} \quad (16)$$

where α_{ver} is the internal angle at the ver -th vertex of a given triangle. The presence of the term $\sqrt{|\alpha_{\text{ver}}(\pi - \alpha_{\text{ver}})|}$ at the denominator helps in preventing that some elements with a low value of λ_{el} might get too seriously distorted.

2.3. ELLIPTICAL CRACK IN THE UNBOUNDED MEDIUM

The first example addressed is depicted in Figure 6 and basically consists of an elliptical crack with major semi-axis $a = 1$ cm and minor semi-axis $b = 0.5a$ embedded in a homogeneous cube of side length $2L$ ($L \gg a$) subjected to tractions σ_{33} (fatigue ratio $R = 0$) $\sigma_{33}^{\text{max}} = \sigma_{33}^0$ applied uniformly on the upper and lower surfaces, with $\sigma_{33}^0 = 10 \text{ kN mm}^{-2}$. The elliptical crack forms angle α with the horizontal plane.

The $\alpha = 45^\circ$ configuration is analysed, adopting as material constants: $m = 3.88$, $C = 1.54 \times 10^{-17}$ (the units for C are consistent with Equation (14) when Δa is expressed in cm and ΔK_{eff} in $\text{kN}\sqrt{\text{cm}}$, $B = 1$, $\nu = 0.3$, $E = 10^4 \text{ kN cm}^{-2}$. At each iteration, the maximum crack advancement Δa_{max} is set equal to $0.25b$ and a set of eight new quarter-point 9-node

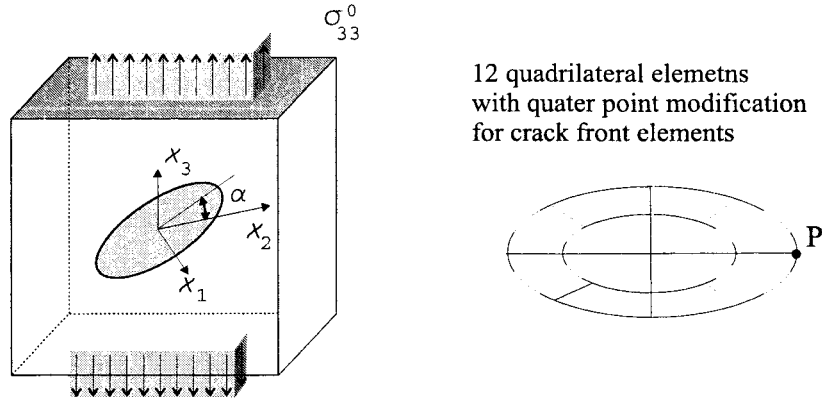


Figure 6. Elliptical crack embedded in a cube and initial mesh adopted.

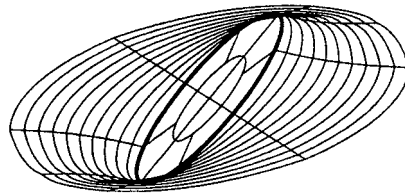


Figure 7. Propagation of an elliptical crack ($\alpha = 45^\circ$): evolution of the crack surface for the first ten increments.

BEs are added ahead of the crack front. For each BE the position of the three nodes lying on the new crack front is chosen according to the criterion specified above; when a node is shared by two elements an ‘averaged’ position is adopted. The quarter-point nodes of the elements lying on the former crack front are moved to usual middle-element positions, and the relevant entries in the coefficient matrices are updated.

The crack front rapidly evolves towards a plane perpendicular to the applied tractions; K_{II} tends to zero, as a natural consequence of the propagation criterion adopted, while K_{III} , though decaying, is less sensitive to the propagation process, as evidenced in Figure 8.

2.4. CORNER CRACK

An elastic cube ($E = 10^4 \text{ kN cm}^{-2}$, $\nu = 0.3$) with an edge crack is submitted to tractions σ_{33} (fatigue ratio $R = 0$, $\sigma_{33}^{max} = \sigma_0$) applied uniformly on the upper and lower surfaces (see Figure 9). The crack middle surface is the intersection of the cube with a circle centered at A , with radius $R = 2 \text{ cm}$ and normal vector $(-1, -1, 2)$. The cube side length is $H = 10 \text{ cm}$ and parameters in Paris law have been chosen as $m = 2.5$, $C = 1.5 \times 10^{-17}$ (as in the previous case, the units for C are consistent with Equation (14) when Δa is expressed in cm and ΔK_{eff} in $\text{kN}\sqrt{\text{cm}}$).

In Figure 9b the outer surface mesh is depicted (312 Q9 elements), while Figure 10a presents a view of the cube interior and of the edge crack (20 standard Q9 elements) as seen from the viewpoint (5, 10, 5) (the reference-system origin is placed in the corner node C).

Figures 10 and 11, on the contrary, display the surface and crack meshes after the first seven increments, along with the stress intensity factor K_I distribution along crack front. The fatigue life of the cracked bar is also displayed: the ‘equivalent’ crack length, obtained as the

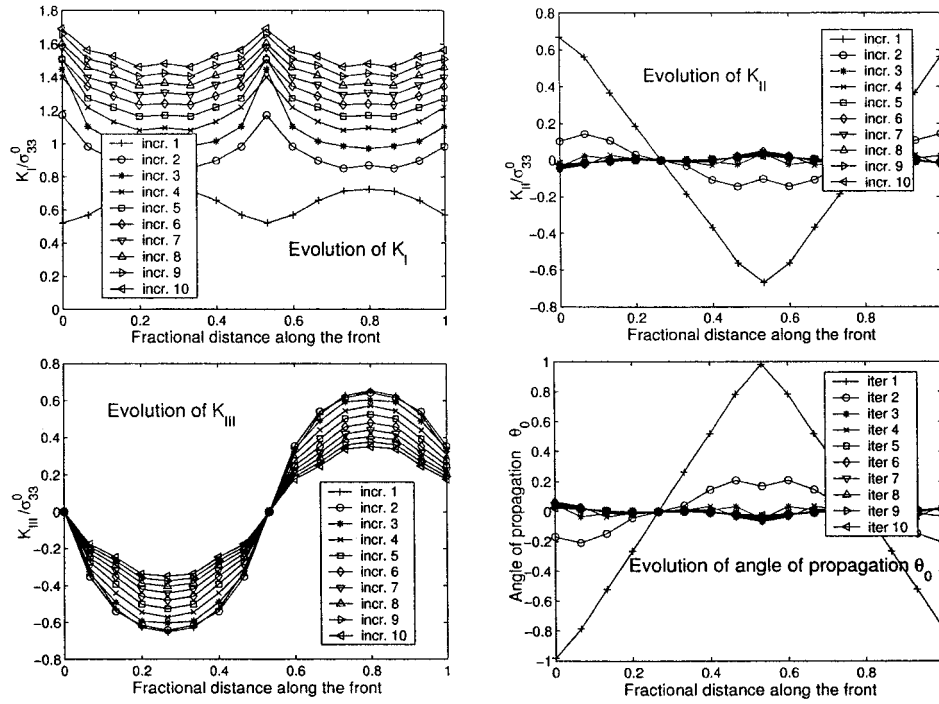


Figure 8. Propagation of an elliptical crack: K_I , K_{II} , K_{III} and θ_0 peak values at nodes along the crack front; the arc length along the front is measured starting at **P** in Figure 6.

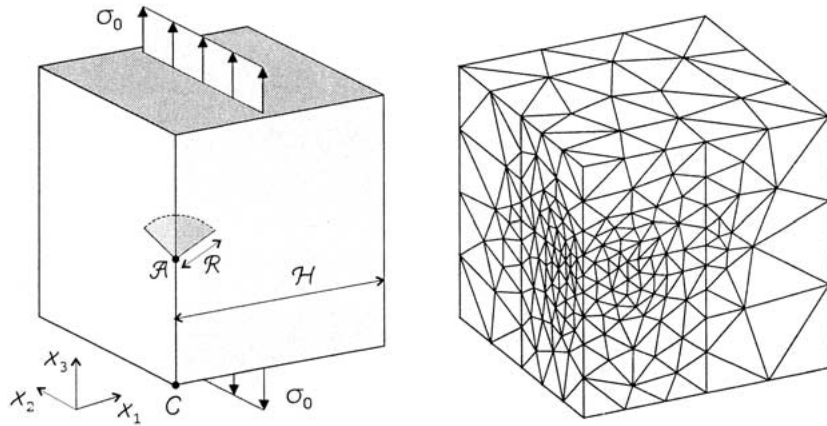


Figure 9. Elastic cube with an edge crack and surface mesh adopted.

sum of the maximum crack advancement at each iteration, is plotted versus the number of cycles.

2.5. SEMICIRCULAR FACE CRACK IN A CUBE

The same analyses have been performed for the semicircular surface crack (of radius $R = 1.5$ cm) of Figure 12 embedded in an elastic cube with material properties as in the previous example. The crack plane makes an angle $\alpha = 45^\circ$ with the $x_1 - x_2$ plane.

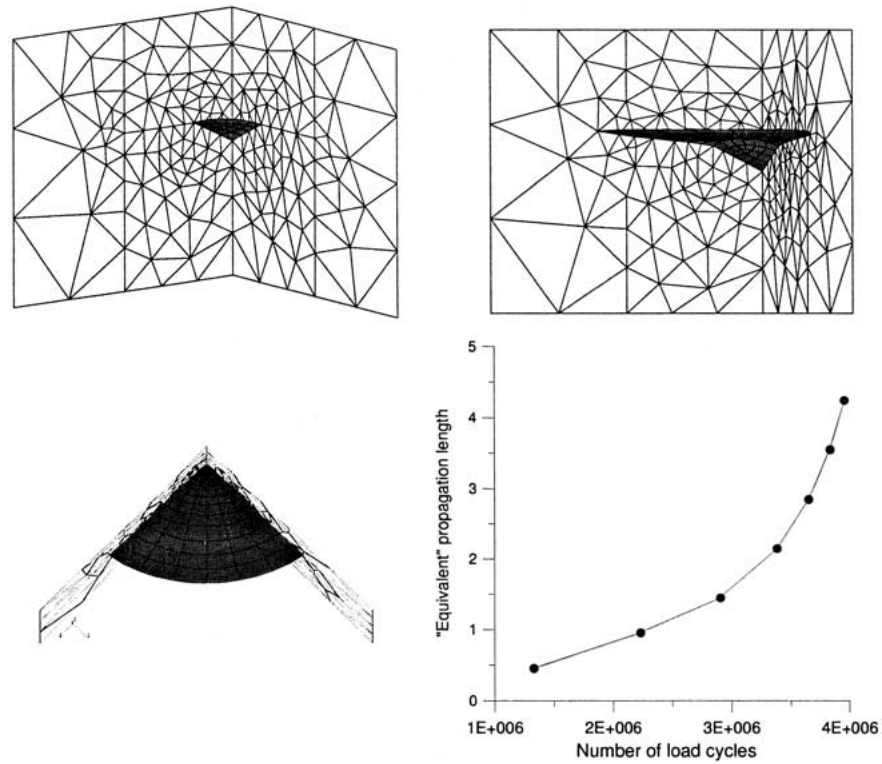


Figure 10. Edge crack after six increments: different views of propagated crack from the cube interior and fatigue life of the bar.

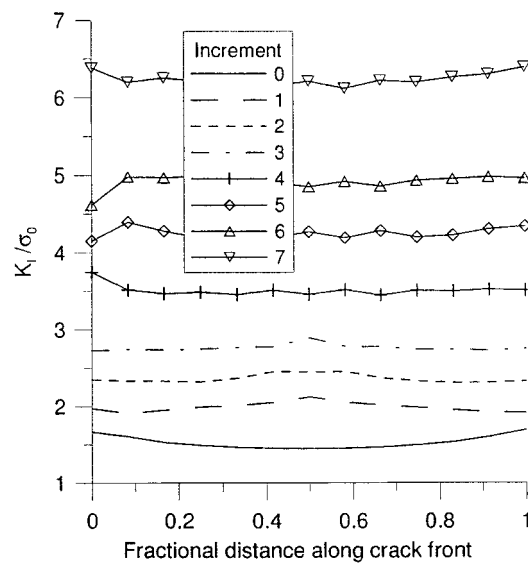


Figure 11. Peak values of the stress intensity factor distributions along crack front for the first six crack extensions

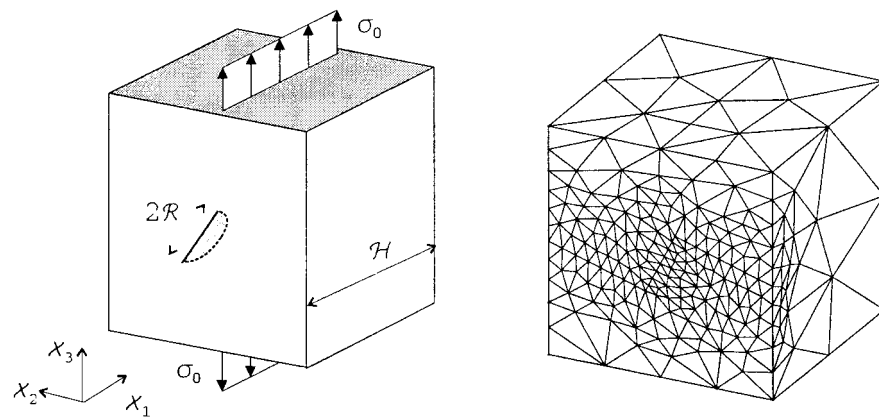


Figure 12. Elastic cube with a semi-circular surface crack and surface mesh adopted.

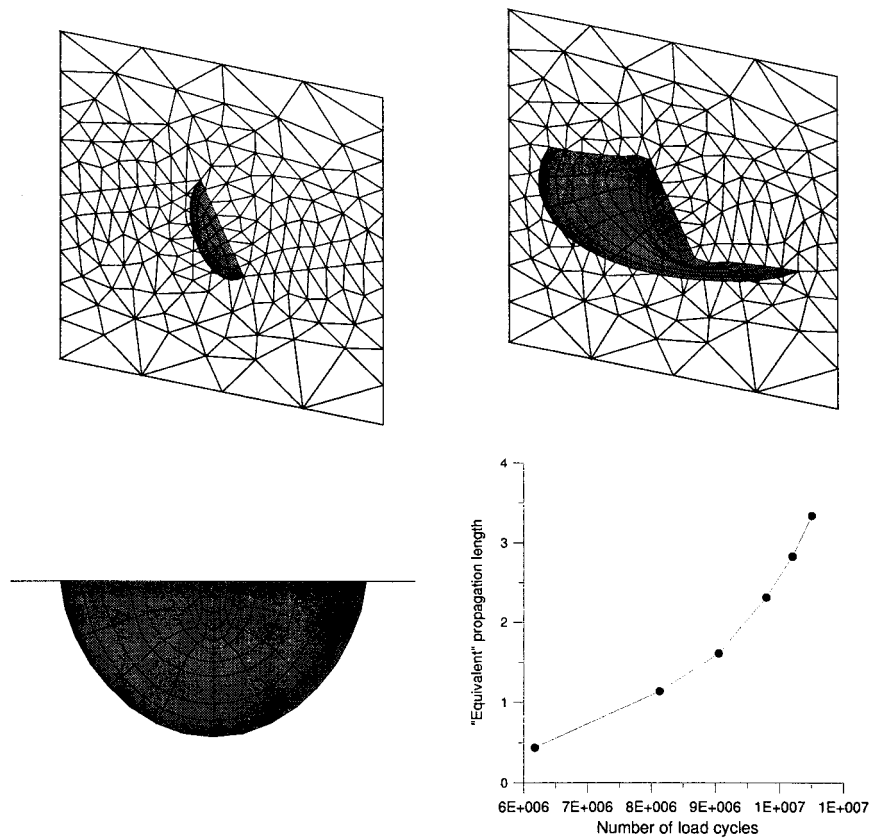


Figure 13. Semicircular surface breaking crack after six increments: different views of propagated crack from the cube interior and fatigue life of the bar.

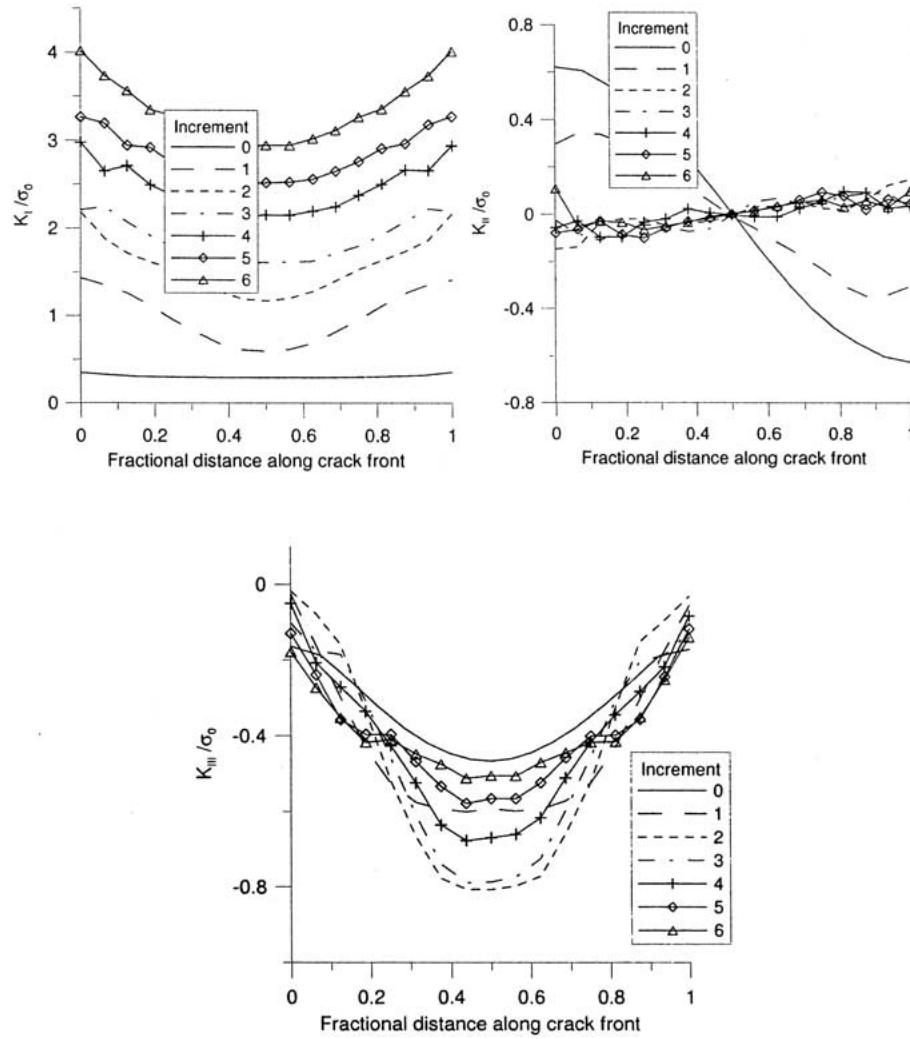


Figure 14. Peak values of the stress intensity factor distributions along crack front for the first six crack extensions.

290 standard Q9 elements have been employed for the outer surface, while the initial crack has been meshed with 24 Q9 elements. Results for the first six increments are collected in Figures 13 and 14.

In both cases the fracture front tends to assume a circular shape and to dispose itself in a plane perpendicular to applied stresses.

3. Remarks and conclusions

The numerical method implemented proves efficient and reliable. However, a more realistic simulation of crack propagation requires taking into account a number of issues pertaining both to the physics underlying fracture processes in 3D and to the numerical solution of large scale problems.

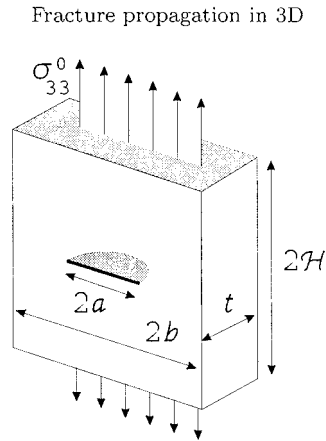


Figure 15. Plate containing a semi-circular surface crack.

3.1. ASYMPTOTIC BEHAVIOUR AT ‘SURFACE POINTS’

Let us consider, for instance, a node P where the crack front intersects the specimen surface.

The asymptotic behaviour of the displacements at P does not reflect, in general, classical Williams’ expansions, due to the discontinuity in the front geometry (see e.g. Pook, 1994). Indeed $u \propto r^\gamma$, where γ depends on the Poisson’s coefficient and on the angle α between the crack front line and the outer surface. The classical stress intensity factors, defined under the assumption of the usual \sqrt{r} behaviour, either approach to zero or diverge (according to whether γ is greater or smaller than 0.5) in a boundary ‘layer’ near point P the thickness of which strongly depends on the problem geometry.

Let us consider, for instance, a semi-circular edge crack in a plate under tension analysed by the symmetric Galerkin BEM. For this testcase well known FEM results are available (Raju and Newman, 1979).

The geometry of the problem is shown in Figure 15; uniform tensile stresses are applied at two opposite faces of the bar (plate) in the direction perpendicular to the crack; a value of Poisson’s ratio $\nu = 0.3$ is adopted.

The configuration considered is characterized by the geometric ratios $H/a = 5$, $b/a = 5$ and $a/t = 0.4$.

The problem is addressed using the three meshes, Mesh A, Mesh B and Mesh C, depicted in Figure 16, having 12, 24 and 40 elements along the circular crack front, respectively. The results obtained in terms of mode-I SIF are plotted in Figure 17a as a function of the angular parameter $2\phi/\pi$ (with $\phi = 0$ at the free surface) and they are compared to the finite element results of Raju and Newman (1979).

From Figure 18 it turns out that the analyses carried out by the SGBEM (in particular with the refined Mesh C) predict a much thinner boundary layer than in Raju and Newman (1979). SIF values far from the external surface are not significantly affected by the mesh refinement and can be accurately evaluated using even rather coarse meshes. Very similar results have been obtained for the two examples of the previous section. When the mesh is fine enough to resolve the boundary layer and a ‘local’ criterion is adopted for predicting crack growth direction and extension, spurious oscillations might originate in the crack geometry requiring frequent smoothing of the crack front. Moreover, such phenomena are amplified by quarter point elements, since they artificially enforce a singularity which does not reflect the actual

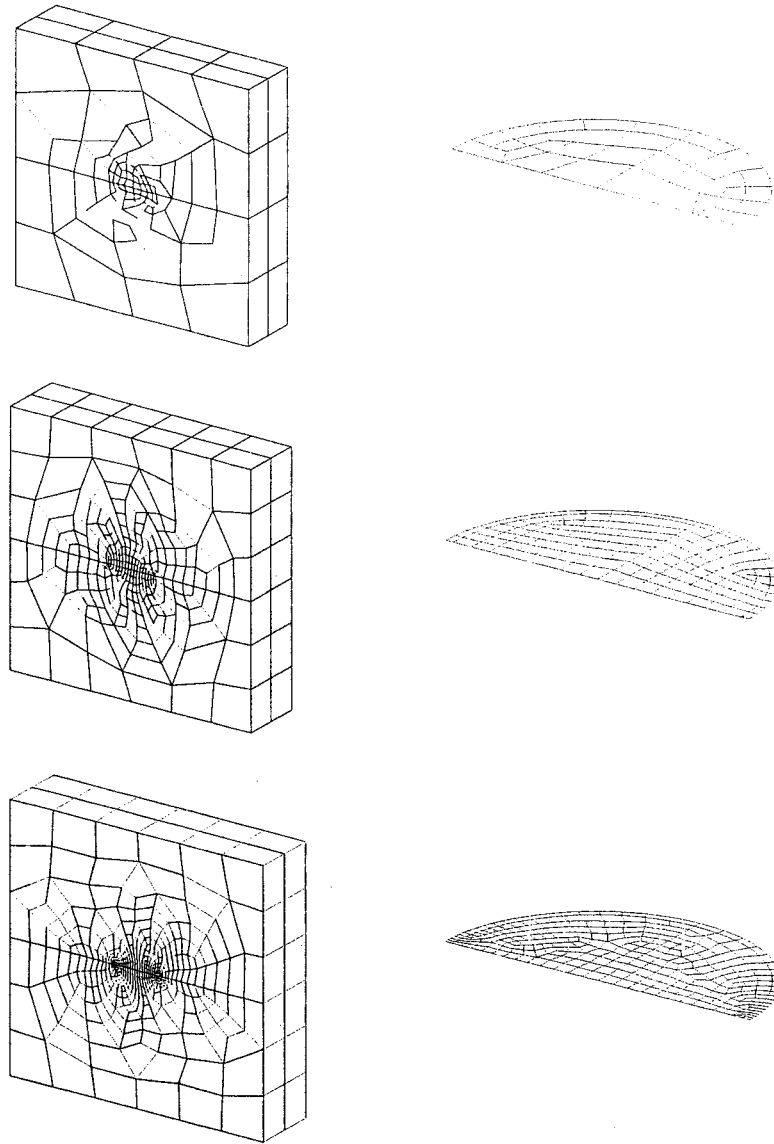


Figure 16. Meshes A, B and C.

local structural response. This is not the case with the rather coarse meshes of Section 2 where only standard elements are employed: no oscillations are induced and smoothing does not prove necessary.

A general and robust numerical approach for ‘curing’ such local effects is still lacking. Indeed, in cases similar to those analysed in the previous section (with boundary layers of negligible dimensions) the results seem to be primarily governed by the angle at which the crack front intersects the outer surface, since it greatly influences the order of singularity (see Pook, 1994). Unfortunately, such an angle cannot be accurately determined by numerical means.

It should be anyway recalled that, when addressing different geometries (see e.g. Frangi *et al.*, 2002), boundary layers of non negligible thickness might be obtained. In order to

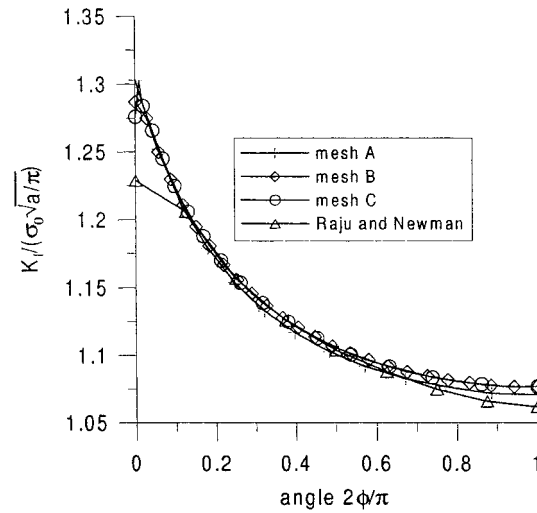


Figure 17. Normalized stress intensity factor for semi-circular surface crack in a plate as function of angular position along crack front; results for the meshes A, B and C and earlier FE results of Raju and Newman (1979).

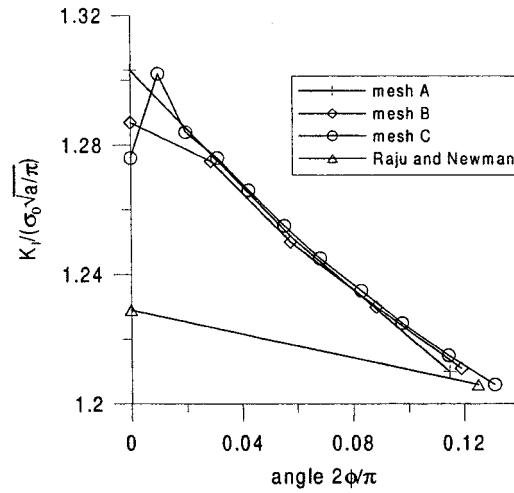


Figure 18. Normalized stress intensity factor for semi-circular surface crack in a plate: 'boundary layer' effect for meshes A, B and C and earlier FE results of Raju and Newman (1979).

account for this and other similar phenomena the material resistance to crack growth (as measured for instance by C in Equation (14)) is sometimes given in the literature (see e.g. Thomson and Sheppard, 1992) by a relation such as $C_p = Q_C^n A$, where C_A is the crack growth resistance at a crack front point inside the body and Q is a material parameter. However, this approach does not generally provide a satisfactory solution since the difficult task calibrating of Q^n is somehow arbitrary.

On the contrary, it is the author's opinion that the adoption of global 'energy' approaches (like, e.g. the minimization of the total potential energy) might lead to better results and are currently under investigation.

3.2. CONSTITUTIVE AND NUMERICAL ISSUES

Another key factor, besides residual stress fields due to (thermal) treatments, is the combined presence of different fracture modes. Mixed *I-III*, *I-II* modes have been the subject of a number of investigations (see e.g. Brown *et al.*, 1985) showing that the propagation direction is strongly dependent on the relative influence of the modes. Branching, ‘factory roof’ cracks are alternative propagation possibilities that the numerical algorithm should be able to simulate, possibly following, also in this case, an energy-based approach. Work along these guidelines is in progress.

From the numerical standpoint, the SGBEM, like all BEM approaches, entails fully populated coefficient matrices. For the viability of the SGBEM in large-scale problems it is mandatory to reduce the computational cost and memory requirements by making recourse to FEM-BEM couplings and recent algorithms such as fast multipole methods and panel clustering. Several contributions along this line have appeared recently with promising results (e.g. Lage and Schwab, 2000; Yoshida *et al.*, 2001) and are being envisaged for more efficient implementations.

Acknowledgements

A research grant from MURST (Cofinanziamento 2000) is acknowledged

References

- Andrä, H. and Schnack, E. (1997) Integration of singular Galerkin-type boundary element integrals for 3D elasticity, *Numerische Mathematik* **76**, 143–165.
- Balakrishna, C., Gray, L.J. and Kane, J.H. (1994) Efficient analytical integration of symmetric Galerkin boundary integrals over curved elements: elasticity, *Comp. Meth. Appl. Mech. Engng.* **117**, 157–179.
- Bonnet, M., Maier, G. and Polizzotto, C. (1998) Symmetric Galerkin boundary element method, *Appl. Mech. Rev.* **51**, 669–704.
- Bonnet, M. (1993) A regularized Galerkin symmetric BIE formulation for mixed 3D elastic boundary value problems, *Boundary Elements Abstracts & Newsletters* **4**, 109–113.
- Brown, M.W., Hay, E. and Miller, K.J. (1985) Fatigue at notches subjected to reversed torsion and static axial loads, *Fatigue Fract. Engng. Mater. Struct.* **8**, 243–258.
- Cisilino, A.P. and Aliabadi, M.H. (1997) Three-dimensional BEM analysis for fatigue crack growth in welded components, *Int. J. for Pressure Vessels and Piping* **70**, 135–144.
- Frangi, A. and Novati, G. (1996) Symmetric BE method in two dimensional elasticity: evaluation of double integrals for curved elements, *Computat. Mech.* **19**, 58–68.
- Frangi, A. (1998) Regularization of boundary element formulations by the derivative transfer method, in Sládek, V., Sládek, J. (eds.), *Singular Integrals in Boundary Element Methods, Advances in Boundary Elements, chap. 4*, Computational Mechanics Publications, 125–164.
- Frangi, A., Novati, G., Springhetti, R. and Rovizzi, M. (2002) 3D fracture analysis by the symmetric Galerkin BEM, *Computat. Mech.*, **28**, 221–231.
- Erichsen, S. and Sauter, S.A. (1998) Efficient automatic quadrature in 3-D Galerkin BEM, *Comp. Meth. Appl. Mech. Engng.* **157**, 215–224.
- Lage, C. and Schwab, C. (2000) Advanced boundary element algorithms, in Whiteman, J.R. (eds.), *Majelap 1999*, Elsevier, 283–306.
- Li, X. and Keer, L.M. (1992) A direct method for solving crack growth problems I, *Int. J. Solids Struct.* **29**, 2735–2747.
- Li, X. and Keer, L.M. (1992) A direct method for solving crack growth problems Shear mode problems II, *Int. J. Solids Struct.* **29**, 2749–2760.

- Li, S., Mear, M.E. and Xiao, L. (1998) Symmetric weak-form integral equation method for three-dimensional fracture analysis, *Camp. Meth. Appl. Mech. Engng.* **151**, 435–459.
- Mi, Y. and Aliabadi, M.H. (1994) Three-dimensional crack growth simulation using BEM, *Comp. Struct.* **52**, 871–878.
- Mi, Y. (1996) *Three-dimensional Analysis of Crack Growth*, Computational Mechanics Publications, Southampton.
- Pook, L.P. (1994) Some implications of corner point singularities, *Engng. Fract. Mech.* **48**, 367–378.
- Raju, I.S. and Newman, J.C. (1977) Three dimensional finite-element analysis of finite-thickness fracture specimens, *NASA-TN*, D-8414.
- Raju, I.S. and Newman, J.C. (1979) Stress-intensity factors for a wide range of semi-elliptical surface cracks in finite-thickness plates, *Engng. Fract. Mech.* **11**, 817–829.
- Sauter, S.A. and Schwab, C. (1997) Quadrature for hp-Galerkin BEM in 3-d, *Numerische Mathematik* **78**, 211–258.
- Sirtori, S., Maier, G., Novati, G. and Miccoli, S. (1992) A Galerkin symmetric boundary element method in elasticity: formulation and implementation, *Int. J. Num. Meth. Engng.* **35**, 255–282.
- Thomson, K.D. and Sheppard, S.D. (1992) Stress intensity factors in shafts subjected to torsion and axial loading, *Engng. Fract. Mech.* **42**, 1019–1034.
- Carter, B.J., Wawrzynek, P.A. and Ingraffea, A.R. (2000) Automated 3D Crack Growth Simulation, *Int. J. Num. Meth. Engng.* **47**, 229–253.
- Wilde, A. and Aliabadi, M.H. (1999) A 3-D Dual BEM formulation for the analysis of crack growth, *Computat. Mech.* **23**, 250–257.
- Xu, G. and Ortiz, M. (1993) A variational boundary integral method for the analysis of 3-D cracks of arbitrary geometry modelled as continuous distributions of dislocation loops, *Int. J. Num. Meth. Engng.* **36**, 3675–3701.
- Yoshida, K., Nishimura, N. and Kobayashi, S. (2001) Application of fast multipole Galerkin boundary integral equation method to elastostatic crack problems, *Int. J. Num. Meth. Engng.* **50**, 525–547.